Available online at www.sciencedirect.com
ScienceDirect
Journal of Computational Physics 218 (2006) 770–793
JOURNAL OF COMPUTATIONAL PHYSICS
www.elsevier.com/locate/jcp

A Numerical procedure for solving 2D phase-field model problems

Ying Xu *, J.M. McDonough, K.A. Tagavi

Department of Mechanical Engineering, University of Kentucky, 151 RGAN Building, Lexington, KY 40506-0503, USA

Received 23 February 2005; received in revised form 20 February 2006; accepted 9 March 2006
Available online 24 April 2006

Abstract

We present a general 2D phase-field model, but without anisotropy, applied to freezing into a supercooled melt of pure nickel. The complete numerical procedure and details of assigning the numerical parameters are provided; convergence of the numerical method is demonstrated by conducting grid function convergence tests. The physics of solidification problems such as conditions for nucleation and crystal growth rate are discussed theoretically and shown to display at least qualitative agreement numerically. In particular, comparison of the computed critical radius with the theoretical one and the consistency of the computational dendrite structure for different Stefan numbers, the relationship between the growth rate and the Stefan number, etc., with the theoretical and experimental evidence indicate that phase-field models are able to capture the physics of supercooled solidification.

Keywords: Numerical procedure; Phase-field model; Supercooling; Solidification

1. Introduction

The basic idea of "phase field" was initiated in the late 1970s. Numerous studies introducing phase-field models were reported in the 1980s leading to increased interest in solving phase transition problems. Fix [1] proposed a method in 1983 including two important effects, surface tension and supercooling, not captured in classical Stefan problems. Surface tension is a stabilizing factor, while supercooling tends to amplify any perturbation introduced in the system. Presence of surface tension and supercooling imposes certain difficulties for numerical solution of Stefan problems, and early attempts to remove the difficulties were not very successful. In [1], Fix introduced a phase variable, a so-called order parameter, ϕ, in his model that is to be determined by an appropriate field equation and varies sharply but smoothly from one value to another over the solid–liquid interface. Langer [2] presented a simple, intuitive description of the phase-field model without proposing any numerical solution approach; and Caginalp and Fife [3] introduced a phase-field model that incorporated

* Corresponding author.
E-mail addresses: yxu2@uky.edu (Y. Xu), jmmcd@uky.edu (J.M. McDonough), kaveh@engr.uky.edu (K.A. Tagavi).
URL: http://www.engr.uky.edu/~acfd (J.M. McDonough).

0021-9991/$ - see front matter
doi:10.1016/j.jcp.2006.03.007

surface tension, anisotropy, curvature and dynamics of the interface along with supercooling by employing the Landau–Ginzburg [4] approach. Later, Caginalp [5] showed that as a limiting case of continuous representation of phase transitions based on microscopic considerations, the phase-field equations can lead to the sharp-interface models, e.g., classical Stefan models, modified Stefan models, Hele–Shaw models and the Cahn–Allen model [5]. He and Socolovsky [6] also showed in detail that the sharp-interface problem arising from any of the major phase transition problems (classical or modified Stefan problem, etc.) can be recovered mathematically by using the phase-field approach as a numerical method to smooth solutions over a thin interface with finite thickness, in which effects of surface tension and supercooling are included. Therefore, the phase-field method converts the sharp interface problem to a stiff system of partial differential equations for evolution of phase and temperature fields. In 1990, Penrose and Fife [7] derived a "thermodynamically-consistent" phase-field model using an analogous entropy functional instead of the Landau–Ginzburg free energy functional. A "thermodynamically-consistent" phase-field model based on the first and second laws of thermodynamics was also presented by Wang et al. [8].

In general, phase-field models provide a method to solve time-dependent free-boundary problems without explicit front-tracking of the interface position. In phase-field models, an additional variable, phase field ϕ, is introduced to explicitly label the solid–liquid interface. For example, if $\phi = 0$ represents the solid, and $\phi = 1$ represents the liquid, then ϕ between 0 and 1 corresponds to the interface region. Therefore, an extra equation, the phase equation, must be derived and subsequently solved in addition to, and simultaneously with energy equation. A mathematical formulation for phase transition problems considered in a region $\Omega \subset \mathbb{R}^d$, $d = 1, 2$ and $t \in \mathbb{R}^1_+$ with an interface $\Gamma(t) \subset \Omega$ is presented in dimensional form:

$$T_t = \alpha \Delta T \quad \text{in } \Omega \setminus \Gamma(t), \tag{1a}$$

$$\rho L_0 v = (k_S \nabla T_S - k_L \nabla T_L) \cdot \boldsymbol{n} \quad \text{on } \Gamma(t), \tag{1b}$$

$$T = T_m - \gamma\kappa - \frac{v}{\mu} \quad \text{on } \Gamma(t). \tag{1c}$$

Here T, α, ρ and L_0 are temperature, thermal diffusivity, density and latent heat at the equilibrium melting temperature T_m, respectively; $\gamma = \sigma T_m/\rho L_0$ is the interfacial energy with σ denoting surface tension; k_S and k_L are thermal conductivities in solid and liquid, respectively; κ is the sum of principal curvatures at a point on the interface; μ is interfacial kinetic coefficient; $\boldsymbol{n}$ is the unit normal to Γ (in the direction from solid to liquid), and v is the normal velocity of a point on the interface. Subscripts S and L represent solid and liquid, respectively; Δ is the Laplacian, and the subscript t denotes partial differentiation with respect to time. The above equations are based on the mathematical model described in [9,10]. Other similar models can be found in [5,6] in dimensionless form.

It is worth mentioning that Karma and Rappel [11,12] developed a "thin-interface" limit of the phase-field model. This is intended to circumvent two limitations of the phase-field approach, namely, necessity of non-zero interface kinetics and computational complexity, to a large degree by modifying the expression for the inverse of kinetic coefficient. In dimensional form the modified result is

$$\beta = \frac{c_p}{\mu L_0} - a_2 \frac{\delta}{\alpha}, \tag{2}$$

where δ is an interface thickness parameter, and a_2 is a positive constant of order unity that depends on the choice of functional forms in phase-field model. By way of contrast, in Caginalp's asymptotic analysis [5] the following simpler expression was obtained:

$$\beta = \frac{c_p}{\mu L_0}. \tag{3}$$

Here we have used notation of the current paper, but Eqs. (2) and (3) are equivalent (modulo notation) to the corresponding ones in [12,5], respectively.

This thin-interface limit has two computational advantages compared with currently used phase-field models: first, it is able to perform simulations with a larger δ/d_0 ratio (where $d_0 = c_p \sigma T_m/\rho L_0^2$ is the capillarity length), which reduces the computation time, especially when the degree of supercooling is small, since it allows larger spatial step; second, the inverse of the kinetic coefficient, β, can be made zero or even negative,

permitting simulation of negligible interface kinetics cases, especially important for metallic systems with fast kinetics. Later, McFadden et al. [13] applied the asymptotic methodology in [12] to a phase-field model with unequal conductivities derived using a thermodynamically consistent approach. They also compared scalings of surface tension and kinetics between classical asymptotic analysis [5] and thin-interface analysis [12]. They found that as interfacial thickness tends to zero, surface tension and kinetics effects remain fixed with the classical asymptotic analysis, while they vanish for the thin interface analysis.

Initially most researchers focused on pure substances in the 2D case and did not consider convection induced by a velocity field or small-scale fluctuations. But phase transitions in binary alloys and solidification in the presence of convection has attracted increasing interest. Kobayashi [14] introduced "a kind of phase field model" to simulate directional solidification and dendritic crystal growth with and without anisotropy. He also investigated stability of the shape of interfaces against noise by introducing low-amplitude random fluctuations. Wheeler et al. [15] applied the phase-field model to a one-dimensional spherically-symmetric geometry and a planar two-dimensional rectangular region to numerically simulate a solid front growing into a supercooled melt. Wheeler et al. [16] also presented a phase-field model of solute trapping during solidification by introducing a species equation into the phase-field model. Murray et al. [17] presented their computation of dendritic solidification based on the model provided in [8]. The numerical study of Kupferman et al. [18] focused on the asymptotic late-stage growth in the large supercooling limit. In contrast, Juric and Tryggvason [19] simulated dendritic solidification with a somewhat different approach, namely, a front-tracking method related to level sets, thus providing an independent check of numerical predictions. Provatas et al. [20] simulated dendrite growth using the phase-field model employed in [11] at low undercooling. They compared their simulations with experimental data on pivalic acid (PVA) obtained from NASA's USMP-4 isothermal dendritic growth experiment (IDGE) described in detail by Koss et al. [21] finding that time-dependent evolution of a 2D dendrite is self-affine in time, and that the dendrite tip position and maximum dendrite width exhibit a power law dependence on time.

Although numerous studies have been conducted using phase-field methods in this area, specific and detailed attention has seldom been given to the numerical analysis, per se. In particular, it has been typical to present results without citing details of the methods employed, or of numerical parameters used to obtain computed results. Moreover, most of the works have shown convergence with respect to asymptotic analyses, but they have not demonstrated convergence of their numerical solutions to those of the differential equations. This makes the grid-function convergence tests employed herein important because they permit assessment of convergence of the numerical method, per se, and thus deduce accuracy of computed results. The purpose of this paper is to provide a complete numerical simulation of dendrite growth into a supercooled melt and in doing so to carefully present details of the numerical analysis. Furthermore, the physical relevance of phase-field models is demonstrated via ability to capture physical effects such as critical radius, power law dependence on time of interface propagation rate, and the independence of growth rate on interfacial thickness, etc. Since time-splitting methods are efficient for solving multi-dimensional problems by decomposing them into sequences of 1D problems, a δ-form Douglas and Gunn [22] procedure is applied to the phase-field model in a rectangular region. So-called δ-form quasilinearization (see e.g. [23]) is applied to the nonlinear terms of the governing equations. This results in a very efficient, robust, formally second-order accurate procedure that, moreover, is easily parallelized (see [24]).

In the following section, we will present the governing equations of the phase-field model for supercooled solidification, including effects of surface tension, and corresponding boundary and initial conditions in Section 2.1. We then provide detailed derivations of numerical methods, e.g., explicit and implicit schemes in Section 2.2, including the derivations of the δ-form Douglas–Gunn and δ-form quasilinearization procedures employed in the implicit scheme in the context of these equations. In Section 3, results are presented concerning observed order of accuracy of the numerical method and the convergence of our numerical solutions. Section 4 contains computed results for dendrite structures at different times, interfacial growth rate with respect to time, the effect of supercooling on the growth rate, effects on growth rate by varying the free parameter ϵ and effect of different initial solid-phase shapes. Comparisons between experiment and theory are also provided. In a final section, we present some conclusions and suggestions for further research.

2. Analysis

In this section, we first present a mathematically well-posed problem consisting of the governing equations of the phase-field model with boundary and initial conditions, followed by details of the numerical method applied to solve the problem. The physics of solidification, such as the condition required for nucleation and crystal growth rate, is then discussed.

2.1. Governing equations

In this subsection, we introduce the equations of the phase-field model along with the scalings employed to render them dimensionless. Boundary and initial conditions required to formulate a well-posed mathematical problem are also prescribed.

The coupled dimensionless governing equations for phase field and temperature [8] can be written as:

$$\phi_t = m\Delta\phi + \frac{m}{\epsilon^2}\phi(1-\phi)[\phi - 0.5 + 30\epsilon a_0 S\theta\phi(1-\phi)], \tag{4a}$$

$$\theta_t = \Delta\theta - \frac{30\phi^2(1-\phi)^2}{S}\phi_t, \quad x \in \Omega, \ \ t \in (t_0, t_f]. \tag{4b}$$

In the above equations, ϕ is the phase value employed to distinguish solid, liquid and interface. By introducing the length scale w (the geometric size of the domain) and the reference time scale w^2/α (the thermal diffusion time, where $\alpha = k/\rho\ c_p$ is assumed to be a constant, and k is the thermal conductivity which is also constant), dimensionless temperature θ, dimensionless spatial variable $\boldsymbol{x}$, and dimensionless time variable t are defined by

$$\theta = \frac{T - T_m}{T_m - T_0}, \quad \boldsymbol{x} = \frac{\hat{\boldsymbol{x}}}{w}, \quad t = \frac{\hat{t}}{w^2/\alpha}.$$

Here T_0 is the initial temperature; $\hat{\boldsymbol{x}}$ and $\hat{t}$ are the dimensional spatial and time variables, respectively.

In addition, four dimensionless parameters of the isotropic phase-field model are defined as

$$S = \frac{c_p(T_m - T_0)}{L_0}, \quad \epsilon = \frac{\delta}{w}, \quad m = \frac{\mu\sigma T_m c_p}{kL_0}, \quad a_0 = \frac{\sqrt{2}w}{12d_0}.$$

Here S is the Stefan number indicating the intensity of supercooling; ϵ is the dimensionless interface thickness; m is the dimensionless interface kinetics, and a_0 relates the length scale in phase-field model to the capillarity length. As shown in [3], as $\epsilon \to 0$, the phase-field model approaches the modified Stefan model equation (1).

The kinetic coefficient μ is a microscopic physical parameter, and it reflects the kink density at the step and the atom exchange rate at each kink, as described in [25]. Linear variation of the kinetic coefficient with temperature might be reasonable for a molecularly rough interface. However, the kinetic coefficient strongly depends on the orientation of the surface for faceted interfaces [2]. For simplicity, the kinetic coefficient is usually assumed to be a constant because it is difficult to determine its value either theoretically or experimentally.

Ω will be a rectangular domain in the present study, and Neumann boundary conditions given by

$$\frac{\partial\phi}{\partial n} = 0, \quad \frac{\partial\theta}{\partial n} = 0$$

will be imposed on $\partial\Omega$. Initially, a small rectangle Ω_0, $\frac{1}{40}$ of the domain size, is placed in the center of the domain to serve as a seed for initiating solidification, and initial data are prescribed as follows:

$$\theta(x,y) = 0, \quad \phi(x,y) = 0, \quad \text{in } \Omega_0,$$
$$\theta(x,y) = -1, \phi(x,y) = 1, \quad \text{in } \Omega \setminus \Omega_0,$$

where $\Omega_0 \equiv [\frac{39}{80}X_0, \frac{41}{80}X_0] \times [\frac{39}{80}Y_0, \frac{41}{80}Y_0]$, and $\Omega \equiv [0, X_0] \times [0, Y_0]$.

2.2. Numerical method

In this subsection, we first implement both explicit and implicit schemes to make comparisons of total arithmetic and computation times between these two approaches. We then provide an outline of the derivations leading to the discrete form of the 2D coupled nonlinear reaction-diffusion equation (4), followed by the pseudo-language algorithm to perform one time step. But we first briefly note the types of algorithms used by investigators in previous studies. Wheeler et al. [15] employed an alternating-direction implicit method (ADI) for the energy equation (similar to the time-splitting we use herein), and an explicit time-integration scheme for the phase-field equation. Both equations were discretized spatially using second-order finite differences on a uniform grid. In Karma and Rappel's work [12], governing equations were discretized using second-order finite differences, except that the Laplacian of ϕ was approximated using a nine-point formula with nearest and next nearest neighbors to reduce effects of grid anisotropy. The temporal discretization was first-order Euler and second-order implicit Crank–Nicolson schemes for phase-field and energy equations, respectively. Beckermann et al. [26] solved the phase-field and energy equations using the method of Karma and Rappel in [11].

2.2.1. Explicit scheme

We apply forward Euler in time and centered-differencing in space to the governing equations (4). Thus, the accuracy is first-order in time and second-order in space. For convenience the nonlinear terms of the phase field and temperature equations are denoted by $F(\theta,\phi)$ and $G(\theta,\phi)$, respectively, defined as follows:

$$F(\theta,\phi) = \phi(1-\phi)[\phi - 0.5 + C_1\theta\phi(1-\phi)], \tag{5a}$$

$$G(\theta,\phi) = \frac{30\phi^2(1-\phi)^2}{S}\phi_t, \tag{5b}$$

where the time derivative term ϕ_t in Eq. (5b) is obtained from the right-hand side of the phase field equation (4b). Discretization of governing equation (4) yields

$$\delta\phi = m\Delta t\left(D^2_{0,x} + D^2_{0,y}\right)\phi^n + \Delta t C_2 F(\theta^n,\phi^n), \tag{6a}$$

$$\delta\theta = \Delta t\left(D^2_{0,x} + D^2_{0,y}\right)\theta^n - \Delta t G(\theta^n,\phi^n). \tag{6b}$$

Here, $(D^2_{0,x} + D^2_{0,y})$ is formal notation for a second-order centered discrete Laplacian. Hence ϕ^{n+1} and θ^{n+1} at the next time step are obtained from $\phi^n + \delta\phi$ and $\theta^n + \delta\theta$, respectively. For convenience, we have introduced the coefficients C_1 and C_2 defined by

$$C_1 = 30\epsilon a_0 S, \quad C_2 = \frac{m}{\epsilon^2}.$$

The explicit scheme is straightforward and easy to implement; however, it requires smaller time steps than does the implicit scheme to satisfy stability constraints. Moreover, such requirements typically become more stringent as the spatial dimension is increased.

2.2.2. Implicit scheme

In this subsection, we describe in detail the implicit numerical procedures employed in this study. We discretize the governing equation using trapezoidal integration in time and centered-differencing in space (hence, a Crank–Nicolson approach) leading to second-order accuracy both in time and in space. In addition, we implement a δ-form Douglas and Gunn time-splitting method [22] in the current paper. This method is guaranteed to maintain second-order accuracy and stability of the unsplit scheme, and it is very efficient, especially in δ-form. Furthermore, it can be extended to 3D problems in a straightforward way.

Again we define functions F and G as was done in Eq. (5); but now the function G is composed of two parts: one part containing the second derivative terms of ϕ, the other having no such terms. Then G can be expressed as

$$G(\theta,\phi) = C_3 g_1(\theta,\phi) + C_4 g_2(\theta,\phi),$$

where

$$g_1(\theta,\phi) = (\phi^4 - 2\phi^3 + \phi^2)(\phi_{xx} + \phi_{yy}),$$
$$g_2(\theta,\phi) = (\phi^4 - 2\phi^3 + \phi^2)F(\theta,\phi),$$

and C_3 and C_4 are defined by

$$C_3 = \frac{30m}{S}, \quad C_4 = \frac{30m}{S\epsilon^2}.$$

Quasilinearizations of F and G are constructed by Fréchet–Taylor expansion in "δ-form" [23]. Therefore, we have

$$F(\theta,\phi) = F^{(m)} + F^{(m)}_\theta \delta\theta + F^{(m)}_\phi \delta\phi,$$
$$g_1(\theta,\phi) = g_1^{(m)} + g^{(m)}_{1\phi}\delta\phi + g^{(m)}_{1\phi_{xx}}\delta\phi_{xx} + g^{(m)}_{1\phi_{yy}}\delta\phi_{yy},$$
$$g_2(\theta,\phi) = g_2^{(m)} + g^{(m)}_{2\theta}\delta\theta + g^{(m)}_{2\phi}\delta\phi,$$

where the superscript (m) denotes the previous iteration value, with $m = 0$ as an initial guess; then $\delta\theta = \theta^{(m+1)} - \theta^{(m)}$, and $\delta\phi = \delta\phi^{(m+1)} - \phi^{(m)}$. Fréchet derivatives of F, g_1 and g_2 can be expressed as

$$F_\theta = C_1\phi^2(1-\phi)^2,$$
$$F_\phi = 2C_1\theta\phi(2\phi^2 - 3\phi + 2) - 3\phi^2 + 3\phi - 0.5,$$
$$g_{1\phi} = (4\phi^3 - 6\phi^2 + 2\phi)(\phi_{xx} + \phi_{yy}),$$
$$g_{1\phi_{xx}} = \phi^2(1-\phi)^2,$$
$$g_{1\phi_{yy}} = \phi^2(1-\phi)^2,$$
$$g_{2\theta} = C_1\phi^4(\phi^4 - 4C_1\phi^3 + 6C_1\phi^2 - 4C_1\phi + 1),$$
$$g_{2\phi} = \phi^2(1-\phi)^2[2C_1\theta(4\phi^3 - 6\phi^2 + 2\phi) - 7\phi^2 + 7\phi - 1.5].$$

Applying trapezoidal integration to Eqs. (4a) and (4b) simultaneously, and replacing the advanced time level values θ^{n+1}, ϕ^{n+1} with $\delta\theta + \theta^{(m)}$ and $\delta\phi + \phi^{(m)}$, respectively, yields

$$\left[I - \frac{\Delta t}{2}m\left(D^2_{0,x} + D^2_{0,y}\right) - \frac{\Delta t}{2}C_2F^{(m)}_\phi I\right]\delta\phi - \frac{\Delta t}{2}C_2F^{(m)}_\theta I\delta\theta$$
$$= \left[I + \frac{\Delta t}{2}m\left(D^2_{0,x} + D^2_{0,y}\right)\right]\phi^n - \left[I - \frac{\Delta t}{2}m\left(D^2_{0,x} + D^2_{0,y}\right)\right]\phi^{(m)} + \frac{\Delta t}{2}C_2(F^{(m)} + F^n), \tag{7a}$$

$$\frac{\Delta t}{2}\left(C_3g^{(m)}_{1\phi}I + C_4g^{(m)}_{2\phi}I + C_3g^{(m)}_{1\phi_{xx}}D^2_{0,x} + C_3g^{(m)}_{1\phi_{yy}}D^2_{0,y}\right)\delta\phi + \left[I - \frac{\Delta t}{2}\left(D^2_{0,x} + D^2_{0,y}\right) + \frac{\Delta t}{2}C_4g^{(m)}_{2\theta}I\right]\delta\theta$$
$$= \left[I + \frac{\Delta t}{2}\left(D^2_{0,x} + D^2_{0,y}\right)\right]\theta^n - \left[I - \frac{\Delta t}{2}\left(D^2_{0,x} + D^2_{0,y}\right)\right]\theta^{(m)} - \frac{\Delta t}{2}\left[C_3\left(g_1^{(m)} + g_1^n\right) + C_4\left(g_2^{(m)} + g_2^n\right)\right]. \tag{7b}$$

Here $D^2_{0,x}$ and $D^2_{0,y}$ denote second-order centered differences with respect to x and y, respectively, and I is the identity matrix. It should be clear that the right-hand sides of Eqs. (7) are the original discrete equations. Hence, these must approach zero as $m \to \infty$ if the iterations converge, implying that $\delta\theta$, $\delta\phi \to 0$ in this limit.

Note further that in Eq. (7a), the matrix multiplying $\delta\phi$ contains a diagonal matrix $-\frac{\Delta t}{2}C_2F^{(m)}_\phi I$. The treatment of this in a two-level Douglas and Gunn time-splitting procedure is accomplished by combining it with the identity matrix and dividing every term in Eq. (7a) by $1 - \frac{\Delta t}{2}C_2F^{(m)}_\phi$. The same strategy can be applied to the matrix $\frac{\Delta t}{2}C_4g^{(m)}_{2\theta}I$ multiplying $\delta\theta$ in Eq. (7b), i.e., we combine it with the identity matrix and divide every term in Eq. (7b) by $1 + \frac{\Delta t}{2}C_4g^{(m)}_{2\theta}$. We guarantee the diagonal dominance for matrices of $\delta\phi$ in Eq. (7a) and $\delta\theta$ in Eq. (7b) by doing so. Moreover, the coefficient matrix of $\delta\theta$, $-\frac{\Delta t}{2}C_2F^{(m)}_\theta I$, in Eq. (7a) is split into the same two parts. For the matrices of $\delta\phi$ in Eq. (7b), we add and subtract an identity matrix I simultaneously,

and then merge the remaining diagonal matrices into the matrix $C_3 g_{1\phi_{xx}} D_{0,x}^2$ of the first split step. Hence we obtain the Douglas and Gunn time-splitting form as

$$(I + A_{1\phi_1})\delta\phi_1 + A_{1\theta_1}\delta\theta_1 = B_1^n\phi^n + S_1^n, \tag{8a}$$
$$(I + A_{2\phi_1})\delta\phi_1 + (I + A_{2\theta_1})\delta\theta_1 = B_2^n\theta^n + S_2^n, \tag{8b}$$

for the first split step, and

$$(I + A_{1\phi_2})\delta\phi_2 + A_{1\theta_2}\delta\theta_2 = \delta\phi_1, \tag{9a}$$
$$(I + A_{2\phi_2})\delta\phi_2 + (I + A_{2\theta_2})\delta\theta_2 = \delta\theta_1, \tag{9b}$$

for the second split step. In Eqs. (8) and (9) the various coefficients are defined as follows:

$$A_{1\phi_1} = -\frac{m\Delta t}{2 - \Delta t C_2 F_\phi^{(m)}} D_{0,x}^2,$$
$$A_{2\phi_1} = \frac{\left[\Delta t\left(C_3 g_{1\phi}^{(m)} + C_4 g_{2\phi}^{(m)} - C_4 g_{2\theta}^{(m)}\right) - 2\right] I + \Delta t C_3 g_{1\phi_{xx}}^{(m)} D_{0,x}^2}{2 + \Delta t C_4 g_{2\theta}^{(m)}},$$
$$A_{1\theta_1} = A_{1\theta_2} = -\frac{\Delta t C_2 F_\theta^{(m)}}{4 - 2\Delta t C_2 F_\phi^{(m)}} I,$$
$$A_{2\theta_1} = -\frac{\Delta t}{2 + \Delta t C_4 g_{2\theta}^{(m)}} D_{0,x}^2,$$
$$A_{1\phi_2} = -\frac{m\Delta t}{2 - \Delta t C_2 F_\phi^{(m)}} D_{0,y}^2,$$
$$A_{2\phi_2} = \frac{\Delta t C_3 g_{1\phi_{yy}}^{(m)}}{2 + \Delta t C_4 g_{2\theta}^{(m)}} D_{0,y}^2,$$
$$A_{2\theta_2} = -\frac{\Delta t}{2 + \Delta t C_4 g_{2\theta}^{(m)}} D_{0,y}^2,$$

and

$$B_1^n = \frac{2I + m\Delta t\left(D_{0,x}^2 + D_{0,y}^2\right)}{2 - \Delta t C_2 F_\phi^{(m)}},$$
$$B_2^n = \frac{2I + \Delta t\left(D_{0,x}^2 + D_{0,y}^2\right)}{2 + \Delta t C_4 g_{2\theta}^{(m)}},$$
$$S_1^n = \frac{-\left[2I - m\Delta t\left(D_{0,x}^2 + D_{0,y}^2\right)\right]\phi^{(m)} + \Delta t C_2(F^{(m)} + F^n)}{2 - \Delta t C_2 F_\phi^{(m)}},$$
$$S_2^n = -\frac{\left[2I - \Delta t\left(D_{0,x}^2 + D_{0,y}^2\right)\right]\theta^{(m)} + \Delta t\left[C_3\left(g_1^{(m)} + g_1^n\right) + C_4\left(g_2^{(m)} + g_2^n\right)\right]}{2 + \Delta t C_4 g_{2\theta}^{(m)}}.$$

The implementation of these formulas can be summarized as a pseudo-language algorithm presented below.

Algorithm 1. Suppose n time steps have been computed using Eqs. (8) and (9) as approximations to Eqs. (4). To advance the numerical solution to time level $n + 1$, carry out the following steps.

1. Set initial values for $\phi^{(m)}$ and $\theta^{(m)}$ to ϕ^n, θ^n, respectively.
2. Set quasilinear iteration counter $m = 0$.
3. Solve the first time-split step, Eqs. (8a), (8b) for ϕ and θ to obtain $\delta\phi_1$ and $\delta\theta_1$.

4. Solve the second time-split step, Eqs. (9a), (9b) for ϕ and θ to obtain $\delta\phi_2$ and $\delta\theta_2$.
5. Update solutions:
   $\phi^{(m+1)} = \phi^{(m)} + \delta\phi_2$,
   $\theta^{(m+1)} = \theta^{(m)} + \delta\theta_2$.
6. Compute iteration error for $\phi^{(m+1)}$ and $\theta^{(m+1)}$:
   If error $<$ convergence tolerance10^{-8}
      go to 7
      else if $m >$ maximum iteration number 300
      print "quasilinear iteration does not converge," exit
   else $m = m + 1$, go to 4
7. Set $n = n + 1$; go to 1 to begin next time step.

We remark here that splitting errors that are often of concern for linear problems are automatically removed by the nonlinear iterations of this algorithm because it is convergence of the unsplit equations that is tested.

2.3. Physics of solidification

In this final subsection, we provide a description of the physics that the phase-field model must capture. Kurz and Fisher [27] note that solidification generally occurs in two stages: the first stage is nucleation controlled, and the second is growth controlled. Once nucleation has occurred, atom transfer to the crystals must continue in order to ensure their growth, which if successful begins the second stage. In Section 2.3.1 we consider nucleation, and in Section 2.3.2 we discuss the dendrite growth rate of the second stage.

2.3.1. Conditions for onset of nucleation

A phase transition (e.g., transition from liquid to solid) is usually initiated by a nucleation process, which proceeds via rearrangement of atoms to form a new crystal structure. Nucleation of a crystal from its melt depends mainly on two processes: thermal fluctuations which lead to the creation of variously sized crystal embryos, and creation of an interface between the liquid and the solid [27]. Hence, the critical condition for nucleation of a spherical nucleus is derived by summing the volume and interface terms for the Gibbs free energy (see [27,28]):

$$\Delta G = \Delta G_{\mathrm{I}} + \Delta G_{\mathrm{V}} = 4\pi r^2\sigma + \frac{4\pi r^3}{3}\Delta g_{\mathrm{V}},$$

where r is the radius of a 3D spherical nucleus, and σ is the surface tension; Δg_{V} denotes the Gibbs free energy of formation per unit volume of the new phase. If Δh_{V} and Δs_{V} represent changes in enthalpy and entropy, respectively, associated with the formation of a unit volume of a new phase, with $\Delta h_{\mathrm{V}} = -L_{\mathrm{f}}$ at the melting temperature T_{m}, and assuming that the difference in specific heat between the liquid and solid is negligible (i.e., $\Delta c_{\mathrm{p}} = 0$) we deduce that [28]

$$\Delta g_{\mathrm{V}} = -L_{\mathrm{f}}\frac{\Delta T}{T_{\mathrm{m}}}.$$

Here, L_{f} is the heat of fusion per unit volume, and $\Delta T = T_{\mathrm{m}} - T$ represents the degree of supercooling of liquid. Therefore, the critical radius r^* is

$$r^* = \frac{2\sigma T_{\mathrm{m}}}{L_{\mathrm{f}}\Delta T}, \tag{10}$$

which means ΔG achieves a maximum as $r \to r^*$ when $T < T_{\mathrm{m}}$ ($\Delta T > 0$). For $r > r^*$, the formation of a nucleus of increasing size results in stabilization of the solid phase. Conversely, for $r < r^*$, a nucleus will shrink and then disappear. The corresponding 2D critical radius can be shown to be

$$r^* = \frac{\sigma T_m}{L_f \Delta T}. \tag{11}$$

We well employ this result herein for comparison with 2D simulations.

2.3.2. Dendrite growth rate

Once a nucleus is formed, it will continue to grow. The growth rate is limited by the kinetics of attachment of atoms to the interface, capillarity and diffusion of heat and mass [27]. In other words, the crystal growth rate depends on the net difference between the rates of attachment and detachment of atoms at the interface. Moreover, it depends on diffusion rate in the liquid and the interface roughness on microscopic scales. Cahn [29] has shown theoretically that there are two major mechanisms related to crystal growth: stepwise and continuous. The mechanism that actually occurs for a specific interface depends on the (thermodynamic) driving force and diffuseness of the interface. Cahn et al. [30] have identified three different regimes according to magnitude of the driving force: classical regime, transitional regime and continuous regime which correspond to low driving force (lateral mechanism), intermediate driving force (lateral spreading mechanism) and high driving force (continuous mechanism), respectively. They also presented expressions for the growth rate in the three regimes. Here, we introduce the expressions only for classical and continuous regimes for simplicity; the transitional regime is more complicated because of the necessity to determine the transition undercooling.

In the classical regime the Gibbs free energy is given by

$$G = \frac{\beta(1 + 2\sqrt{g})}{g} \frac{DL^2 \Delta T^2}{4\pi R T^3 \sigma V_m},$$

or

$$G = \frac{\beta D L^2 \Delta T^2}{4\pi g \sigma R T^3 V_m} \quad \text{for } g \ll 1, \tag{12}$$

where g is the diffuseness parameter ($g \sim 1$ implies that the interface is sharp); L is the latent heat of fusion per mole, with V_m the molar volume of solid, a the step height and R the gas constant (see [31]). In the continuous regime

$$G = \frac{\beta D L \Delta T}{a R T^2}, \tag{13}$$

The assumption that the transport process by which molecules add to the solid at the step is related to liquid diffusion introduces the parameter β that expresses the degree to which the assumption is not strictly satisfied. An empirical relationship for this parameter is [30]

$$\beta = 6\left(\frac{a}{\lambda}\right)^2 \left(\frac{v_i}{v_l}\right),$$

where λ is the mean jump distance that a molecule moves to the next diffusion step in the liquid, and v_i, v_l are the jump frequencies at the interface and in the liquid, respectively. The growth rate equations (12) and (13) imply a quadratic relation between the growth rate and the degree of supercooling for a lateral mechanism and a linear relation for a continuous mechanism.

3. Numerical convergence tests

In this section, we first provide specific details of physical and numerical parameters employed in the computations. We then present data showing convergence of physical energy of the system as truncation error is reduced and numerical precision is increased, and we display data associated with convergence rate of quasi-linear iterations for two different versions of the overall solution procedure. Finally, we supply specific information associated with grid function convergence.

3.1. Physical and numerical run conditions

Computations were performed on a HP N-4000 SMP, and later on a HP SuperDome, operated by the University of Kentucky Computing Center. The Fortran 90 computer programming language was used with 64-bit arithmetic unless otherwise noted. In the present study, the square domain is chosen to be $\Omega \equiv [0,4] \times [0,4]$ except when specified otherwise. Pure nickel is used as the material, but no anisotropy of the interface is assumed. The thermo-physical parameters of nickel can be found in [32] and are listed in Table 1. For simplicity, we assume that density, specific heat and thermal conductivity are constant, and values in the liquid are equal to those in the solid. Since there is no general strategy for determining the kinetic coefficient μ, we assume that it is of $\mathcal{O}(1)$ for pure metal, and choose $\mu = 2.85$ m/(K s) such that the dimensionless kinetic coefficient m is exactly 0.05 as done by Wheeler et al. [15].

It is clear from Eqs. (4) that $\epsilon \to 0$ represents an extreme singularity of this model, and in this case neither initial nor boundary conditions can be satisfied. Indeed, the semilinear terms of Eq. (4a) dominate. In light of this, one should expect that the unconditional stability of trapezoidal integration for linear constant-coefficient problems will be lost for $\epsilon > 0$ sufficiently small. Moreover, ϵ is required to be in the appropriate range according to values of Δx and Δy. On the one hand, we will lose resolution of the interface, and interface propagation is no longer smooth if ϵ is too small (approximately 10 times smaller than the space step). On the other hand, the interface region becomes mushy if ϵ is too large (see Fig. 1 for details). Fig. 1 presents the choice of ϵ for different space steps. The minimum time step sizes Δt to satisfy stability condition are 6×10^{-6}, 10^{-5}, 2×10^{-5}, 2.2×10^{-5}, 4×10^{-5} and 6×10^{-5} corresponding to $\Delta x = \Delta y = 1.25 \times 10^{-3}$, 2.5×10^{-3}, 5×10^{-3}, 0.01, 0.02 and 0.04, respectively. For $\Delta x = \Delta y = 5 \times 10^{-3}$, it is required that $0.0008 < \epsilon < 0.0047$. In the current computations a fixed $\epsilon = 0.004$ is used to maintain consistency with other authors' work. The length scale is $w = 2.1 \times 10^{-6}$ m, and $a_0 = 400$. The Neumann boundary condition for temperature implies that the domain Ω is adiabatic, i.e., it is an adiabatic and therefore for the present case also an isenthalpic system.

Table 1
Thermo-physical parameters of nickel

Density ρ (kg/m^3)	Specific heat c_p (J/kg K)	Thermal conductivity k (J/m K s)	Surface tension σ (J/m^2)	Melting temperature T_m (K)	Heat of fusion L_0 (J/kg)
8900	656.19	88.5	0.37	1728	292333.9

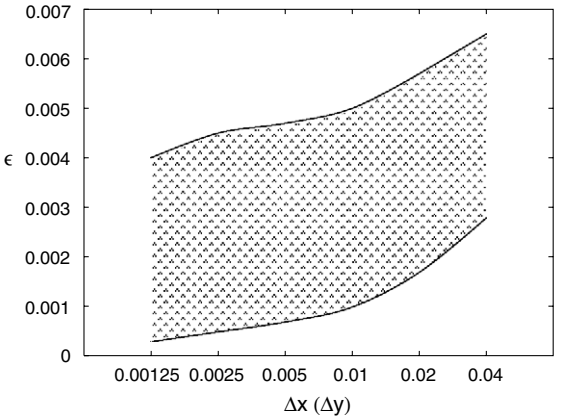

Fig. 1. Semilog plot of ϵ versus Δx and Δy.

3.2. Comparison between explicit and implicit schemes

We have conducted computations using two different types of time integration schemes as explained in Section 2.2. We compared the total arithmetic for one time step and time step size required for stability. We found that although the ratio of total arithmetic between the implicit and explicit schemes is $\mathcal{O}(10)$, the time step size required for stability of the implicit scheme is 10 times greater than that of the explicit scheme with typical space steps $\Delta x = \Delta\ y = 5 \times 10^{-3}$. Moreover, the time step size must be decreased quadratically with linear decrease of spatial step size to maintain stability of the explicit scheme, while the required time step size for the implicit scheme decreases only linearly. We conclude that the explicit scheme is simpler, and it is efficient if the spatial step size is not required to be small. However, since we are solving highly nonlinear equations (Eq. (4a)), and grid sizes should be small enough to capture the details of dendrite structure, the implicit method is superior for the current problem. Moreover, since we will calculate dendrite growth in a flow field (and in three space dimensions) in the future, leading to a need for even finer spatial resolution (and thus more stringent requirements for stability), we choose to emphasize the implicit scheme for our computations.

3.3. Energy conservation and quasilinear iteration convergence

In this subsection, we present results for two specific basic tests performed on the code employing implementation of our implicit method. The first of these checks is basically a physical one: that energy (in the sense of the L^2 norm) is conserved in the discrete calculations. The second involves monitoring convergence rates of the nonlinear iterations required within each time step, thus providing information to allow quantitative assessment of efficiency of the computations.

We compared computed total energy of the system for a fine grid ($\Delta x = \Delta y = 0.005,\ \Delta t = 5 \times 10^{-5}$), a coarse grid ($\Delta x = \Delta y = 0.01,\ \Delta t = 1 \times 10^{-4}$) and using single-precision arithmetic for the coarse grid to verify that energy is conserved in this system. We found that energy of the single-precision coarse grid calculation is decreasing in time, while energies of the coarse and fine grids of the double-precision computations are increasing. Moreover, the rate of energy increase is lower on the fine grid than on the coarse grid for double-precision arithmetic, and the rate of decrease of the single-precision calculation for the coarse grid is greater than the rate of increase of the double-precision calculation on the same grid. We conclude that the energy decrease of single precision for the coarse grid is primarily caused by the truncation error, while the energy increase in this system is caused by the rounding error; so the rate of energy increase is decreased when we refine the grid. We display the error in total energy (absolute value of computed energy difference between current and initial time) caused by energy increasing as a function of spatial step size in Fig. 2, which shows that the total energy error is decreasing and approaching zero as we refine the grid. Therefore, the system energy is conserved to within controllable arithmetic errors. Moreover, Fig. 2 also shows that the energy error

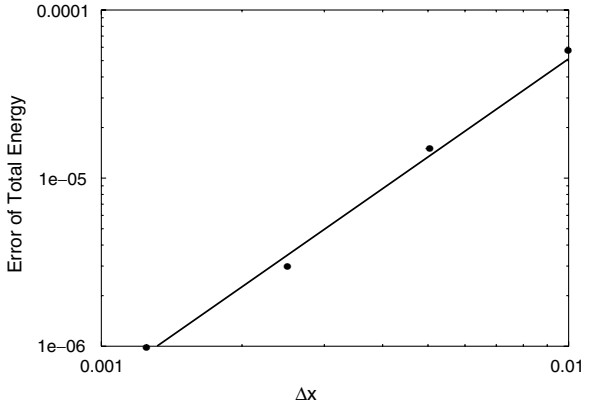

Fig. 2. Total energy error as a function of spatial step size at $t = 0.2$.

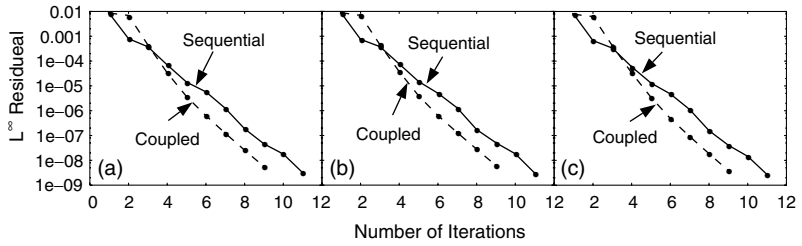

Fig. 3. Comparison of L^{∞} residual with number of iterations for sequential and coupled methods with $\Delta x = \Delta y = 0.01$, $\Delta t = 5 \times 10^{-5}$ and $S = 0.5$ at three different times: (a) $t = 0.05$; (b) $t = 0.1$; (c) $t = 0.2$.

is decreased by a factor four as we refine the space and time step sizes by a factor two, which indicates a second-order accuracy in a weak sense.

To analyze convergence of quasilinear iterations, we compared the computations using a fully-coupled technique (i.e., solving Eq. (8a) coupled with Eq. (8b) followed by solving Eq. (9a) coupled with Eq. (9b)) and a sequential technique (i.e., solving Eqs. (8a), (9a), (8b) and (9b) successively). The comparison of L^{∞} residual as a function of number of iterations per time step shown in Fig. 3 indicates that the Newton–Kantorovich (quasilinearization) convergence rate with convergence tolerance 10^{-8} of the coupled method is greater than that of the sequential method, as might be expected. In addition we observed that the CPU time of the sequential method is approximately 10% greater than that of the coupled method. However, storage needed for the coupled method is much greater than that for a sequential method because we must solve a $n \times n$ block-banded matrix system with each block being a 2×2 matrix for the coupled method rather than a simple $n \times n$ matrix for the sequential method. In the current computations, since the spatial grid spacing should be very small to perform accurate simulations at the interface, large storage is needed. Hence, the sequential method is chosen to reduce this as much as possible.

We also notice that the quasilinear iteration does not converge quadratically but only almost log-linearly (i.e., one decimal place of accuracy is gained with each iteration), as shown in Fig. 3. We conducted several further numerical tests and found that the expected quadratic convergence rate can be achieved if we use smaller time steps. However, computations with a smaller time step caused an increase of CPU time despite the need for fewer iterations per time step. Therefore, we choose to compute with the larger time step which proves to be sufficiently accurate, and stable but leads to more iterations per time step. Fig. 3 displays results at three different times in parts (a)–(c). It is clear that over the observed time interval convergence rate of nonlinear iterations is quite insensitive to the (physical) time at which this is monitored.

3.4. Grid function convergence tests

Grid function convergence tests were conducted using four different combinations of spatial step and time step sizes as shown in Table 2. We start from uniform $h \equiv \Delta x = \Delta y = 0.01$ and $k \equiv \Delta t = 5 \times 10^{-5}$. We then successively decrease h and k simultaneously by a factor of two and compute the L^2 norm of differences on successive grids for ϕ and θ using four different sets of discrete step sizes: h and k, $\frac{h}{2}$ and $\frac{k}{2}$, $\frac{h}{4}$ and $\frac{k}{4}$, $\frac{h}{8}$ and $\frac{k}{8}$, which are denoted by $\|\phi^h - \phi^{h/2}\|$ and $\|\theta^h - \theta^{h/2}\|$, etc., in Table 2. We then compute the ratios $\frac{\|\phi^h - \phi^{h/2}\|}{\|\phi^{h/2} - \phi^{h/4}\|}$, $\frac{\|\phi^{h/2} - \phi^{h/4}\|}{\|\phi^{h/4} - \phi^{h/8}\|}$ and $\frac{\|\theta^h - \theta^{h/2}\|}{\|\theta^{h/2} - \theta^{h/4}\|}$, $\frac{\|\theta^{h/2} - \theta^{h/4}\|}{\|\theta^{h/4} - \theta^{h/8}\|}$ to show convergence in the strong L^2 sense. We notice that the computed order of accuracy is increasing monotonically as we refine the grid, and we are able to obtain essentially second-order accuracy at some fine grid since the theoretical value of four for the error-norm ratios is between the computed values 2.73 and 9.60 for ϕ, and 3.51 and 10.56 for θ.

To explain this apparent "superconvergence" rate, in Fig. 4 we compare a small part of the dendrite surface for four different grid spacings with tic marks indicating actual dendrite surface locations. We display only ϕ because the temperature profile θ is similar. Recall that the leading truncation error for ϕ using centered differencing in space and trapezoidal integration in time is $\frac{1}{12}(\phi_{xxxx}h^2 + \phi_{ttt}k^2)$, where ϕ_{xxxx} and ϕ_{ttt} represent the fourth derivative in space and the third derivative in time, respectively. We notice that the number of dendrite

Table 2
Grid function convergence tests

	h 0.01 k 5×10^{-5}	$\frac{h}{2}$ 0.005 $\frac{k}{2}$ 2.5×10^{-5}	$\frac{h}{4}$ 0.0025 $\frac{k}{4}$ 1.25×10^{-5}	$\frac{h}{8}$ 0.00125 $\frac{k}{8}$ 6.25×10^{-6}
$\|\phi^h-\phi^{h/2}\|$	8.31×10^{-3}		–	–
$\|\phi^{h/2}-\phi^{h/4}\|$	–	3.05×10^{-3}		–
$\|\phi^{h/4}-\phi^{h/8}\|$	–	–	3.17×10^{-4}	
$\frac{\|\phi^h-\phi^{h/2}\|}{\|\phi^{h/2}-\phi^{h/4}\|}$	2.73			–
$\frac{\|\phi^{h/2}-\phi^{h/4}\|}{\|\phi^{h/4}-\phi^{h/8}\|}$	–	9.60		
$\|\theta^h-\theta^{h/2}\|$	8.41×10^{-4}		–	–
$\|\theta^{h/2}-\theta^{h/4}\|$	–	2.40×10^{-4}		–
$\|\theta^{h/4}-\theta^{h/8}\|$	–	–	2.27×10^{-5}	
$\frac{\|\theta^h-\theta^{h/2}\|}{\|\theta^{h/2}-\theta^{h/4}\|}$	3.51			–
$\frac{\|\theta^{h/2}-\theta^{h/4}\|}{\|\theta^{h/4}-\theta^{h/8}\|}$	–	10.56		

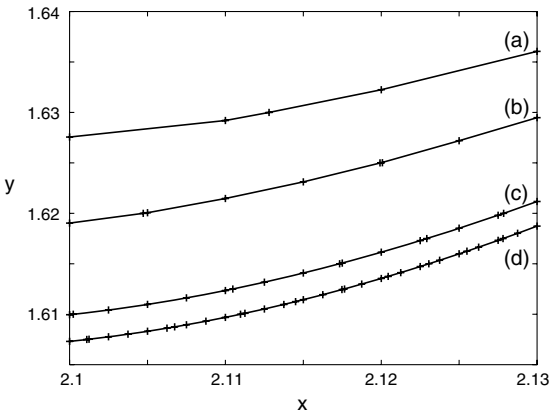

Fig. 4. Dendrite surface locations for four different combinations of space and time step sizes with $S = 0.5$ at $t = 0.05$: (a) $\Delta x = \Delta y = 0.01$, $\Delta t = 5\times10^{-5}$; (b) $\Delta x = \Delta y = 0.005$, $\Delta t = 2.5\times10^{-5}$; (c) $\Delta x = \Delta y = 0.0025$, $\Delta t = 1.25\times10^{-5}$; (d) $\Delta x = \Delta y = 0.00125$, $\Delta t = 6.25\times10^{-6}$.

surface points shown in Fig. 4, together with the fact that number of grid points in the mushy zone increases approximately two times faster than the number of grid points of the total domain when we refine the grid, implies both a smoother solution and a somewhat under estimation of actual grid refinement in precisely the region where most of the truncation error occurs. Hence, the high-order derivatives of ϕ remain bounded, in fact, become small as we refine the grid, and ratios of the L^2 norm continue to increase as we refine the grid. Therefore, the formal second-order accuracy should be obtained, even pointwise for a sufficiently fine grid. In any case, we have demonstrated that solutions to the discrete equations do, in fact, converge to those of the phase-field differential system as discretization step sizes are refined.

4. Computed results and discussions

In this section, we present the dendrite shapes and temperature fields at three different times with initial Stefan number $S = 0.5$ to demonstrate physical realism of the computations. Nucleation conditions and the physics of crystal growth rate are then discussed. Effects of the free parameter ϵ on the interface growth rate are also investigated. Finally, we describe the effect of shape of the initial seed on the final computed dendrite shape.

4.1. Dendrite structures at different times

Figs. 5 and 6 present the interface locations and temperature fields at three different times $t = 0.05$, 0.1 and 0.2 for the Stefan number $S = 0.5$. In Fig. 5, dendrite structures at different times display the end-splitting property during dendrite growth, and exhibit different growth rates of the various interfacial points. In Fig. 6, we notice that the shape of isothermal lines does not follow the interfacial shape. The reason is that the interfacial temperature determined by Eq. (1c) is a function of local curvature and interfacial speed. Therefore, interfacial temperature is not a constant.

We describe the method used to determine the location of interfacial points via Fig. 7. The intersections of grid lines and the fictitious surface $\phi = 0.5$ are considered as points on the interface. The criterion that an interface point must be on the cell wall where the phase field value ϕ is changing from less than 0.5 to greater than 0.5 is applied to determine these intersections. Locations of intersections on a cell wall are computed by linear interpolation of phase field ϕ at two adjacent grid points. Two flags are introduced: one is the counter for the number of interface points in one cell; the other is the label of the cell boundary with or without an interface point. For example, 1 denotes a cell wall containing an interface point; 2 marks a cell wall without an interface point, or with an interface point but for which computations are complete. Finally, 0 corresponds to a new cell wall at which no analysis has yet been done.

Initially all the cell boundaries are labeled as 0. The first step is to locate the interface points in the current cell. For example, we start from grid point $(i-1,j-1)$ in cell (i,j) and choose the bottom boundary as the initial cell wall to be examined; then we proceed in the clockwise direction around the cell boundary. Phase-field values ϕ on grid points $(i-1,j-1)$, $(i-1,j)$ and (i,j) are $\phi > 0.5$, $\phi < 0.5$ and $\phi > 0.5$, respectively. Therefore, there exist two interface points on the boundary of cell (i,j): one is between grid points

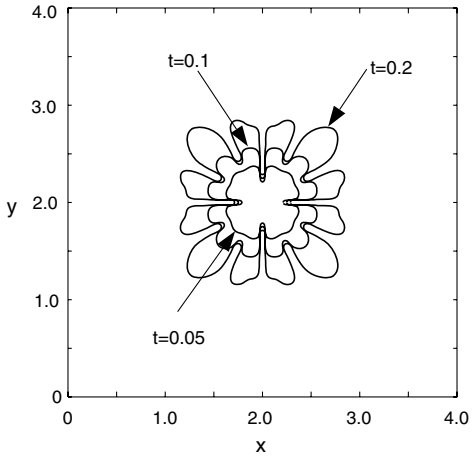

Fig. 5. Dendrite structures for $S = 0.5$ at time $t = 0.05$, $t = 0.1$ and $t = 0.2$ computed with grid spacing $\Delta x = \Delta y = 0.01$, and $\Delta t = 5 \times 10^{-5}$.

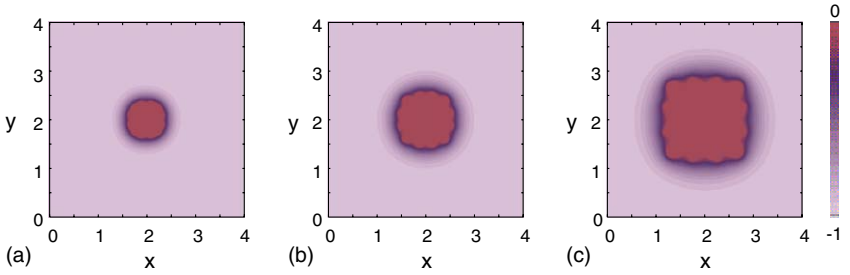

Fig. 6. Temperature fields at (a) $t = 0.05$, (b) $t = 0.1$ and (c) $t = 0.2$.

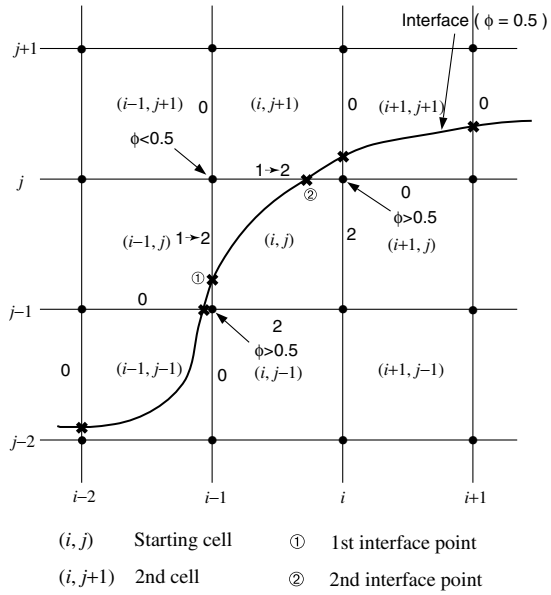

Fig. 7. Interface-point computation sketch.

$(i-1,j-1)$ and $(i-1,j)$, and the other is between grid points $(i-1,j)$ and (i,j). Hence, the left and upper cell boundaries which have interface points on them are labeled as 1; the others (on the same cell) are labeled as 2. Moreover, for cell (i,j), the number of interface points, 2, is stored in an interface-points counter. The second step is to compute the location of interface points ① and ② and the interfacial velocity of each point in the current cell. After the computations, the labels "1" of cell boundaries are changed to "2", preventing interface point ① from being counted again in cell $(i-1,j)$ and interface point ② from being counted a second time in cell $(i,j+1)$. In Fig. 7 "$1 \rightarrow 2$" indicates that the cell wall is labeled as 1 in the first step, then changed to 2 in the second step of the calculations. We now move to the next cell, $(i,j+1)$. This cell is selected based on the last interface point location in the previous cell. For example, the last point on the bottom, left, top and right cell boundary leads to moving to the lower, left, upper and right cell, respectively. It should be mentioned that if the interface is smooth enough, there must be two interface points in each cell through which it passes. Failure of this implies that the grid being employed is not sufficiently refined. Our algorithm prints an error message and moves to the next time step if this is detected. These steps are summarized in the following algorithm.

Algorithm 2. Suppose ϕ and θ have been computed using Eqs. (8) and (9) as approximations to Eqs. (4) at time step n. Label all cell boundaries as 0, and carry out the following steps to determine location of the interface:

1. Start from a grid point (e.g., center point of the domain), check the value of $\phi_{i,j}$ in positive x direction until $\phi_{i-1,j} < 0.5$ and $\phi_{i,j} > 0.5$. Then cell (i,j) is the starting cell.
2. Set point-counter $= 0$
3. If ($\phi_{i-1,j} < 0.5$ and $\phi_{i,j} > 0.5$) or ($\phi_{i-1,j} > 0.5$ and $\phi_{i,j} < 0.5$)
   LabelI$(i-1,j) = 1$,
   point-counter $=$ point-counter $+ 1$
   else
   LabelI$(i-1,j) = 2$
4. If ($\phi_{i-1,j} < 0.5$ and $\phi_{i-1,j+1} > 0.5$) or ($\phi_{i-1,j} > 0.5$ and $\phi_{i-1,j+1} < 0.5$)
   LabelJ$(i-1,j) = 1$,
   point-counter $=$ point-counter $+ 1$
   else
   LabelJ$(i-1,j) = 2$

5. If ($\phi_{i-1,j+1} < 0.5$ and $\phi_{i,j+1} > 0.5$) or ($\phi_{i-1,j+1} > 0.5$ and $\phi_{i,j+1} < 0.5$)
   LabelI($i-1,j+1$) = 1,
   point-counter = point-counter + 1
   else
   LabelI($i-1,j+1$) = 2
6. If ($\phi_{i,j} < 0.5$ and $\phi_{i,j+1} > 0.5$) or ($\phi_{i,j} > 0.5$ and $\phi_{i,j+1} < 0.5$)
   LabelJ(i,j) = 1,
   point-counter = point-counter + 1
   else
   LabelJ(i,j) = 2
7. Check smoothness:
   If point-counter > 2
   print "no smooth interface,"
   go to 12
8. If LabelI($i-1,j$) = 1
   compute interface-point location
   LabelI($i-1,j$) = 2,
   point-counter = point-counter − 1
   If point-counter = 0
   $i = i$,
   $j = j-1$,
   go to 2
9. If LabelJ($i-1,j$) = 1
   compute interface-point location
   LabelJ($i-1,j$) = 2,
   point-counter = point-counter − 1
   If point-counter = 0
   $i = i-1$,
   $j = j$,
   go to 2
10. If LabelI($i-1,j+1$) = 1
    compute interface-point location
    LabelI($i-1,j+1$) = 2,
    point-counter = point-counter − 1
    If point-counter = 0
    $i = i$,
    $j = j+1$,
    go to 2
11. If LabelJ(i,j) = 1
    compute interface-point location
    LabelJ(i,j) = 2,
    point-counter = point-counter − 1
    If point-counter = 0
    $i = i+1$,
    $j = j$,
    go to 2
12. Continue to solve Eqs. (8) and (9) at time level $n+1$

This algorithm works well for a simple interface separating solid and liquid phases but lacks the sophistication needed handle cases for which the solid region is not simply connected.

4.2. Critical initial area

In order to draw an equivalence between the square initial area being treated here and a 2D circular nucleus, we introduce a hydraulic diameter

$$D_h = \frac{4A}{P},$$

where A is the cross-sectional area, and P is the perimeter. Then we rewrite Eq. (11) in the form of side length of the square as

$$\widehat{L}^* = \frac{2\sigma T_{\mathrm{m}}}{L_{\mathrm{f}}\Delta T}.$$

Moreover, the dimensionless critical length is

$$L^* = \frac{2\sigma T_{\mathrm{m}} c_{\mathrm{p}}}{\rho L_0^2 w S}. \tag{14}$$

Hence, the critical lengths are 0.059, 0.030 and 0.020 corresponding to the Stefan numbers 0.01, 0.02 and 0.03, respectively. We use these to verify that the relation between the critical length and the Stefan number obeys Eq. (14) employing discrete step sizes $\Delta x = \Delta y = 0.005$ and $\Delta t = 2.5 \times 10^{-5}$. The results displayed in Figs. 8–10 indicate that there exists a critical length when S is small, and this critical length decreases as S increases. In these figures the left plots show that the solid areas are decreasing as time increases, indicating shrinkage of nuclei; the right ones indicate that the nuclei are growing with time. The computed critical lengths from Figs. 8–10 are in the range of 0.04–0.05, 0.02–0.03 and 0.01–0.02 corresponding to Stefan numbers 0.01, 0.02 and 0.03, respectively, which are essentially the same as the theoretical ones computed from Eq. (14). This consistency of computed critical lengths with theoretical ones suggests that the phase-field model is able to capture the physics of solidification on at least a semi-quantitative basis.

4.3. Growth rate

In this subsection the behaviors of dendrites under various supercoolings are studied, and a comparison of growth rate at different Stefan numbers is presented. In addition, the relationship between growth rate and Stefan number is discussed. The domain size is enlarged to $\Omega \equiv [0,8] \times [0,8]$ to accommodate the larger dendrites that occur when Stefan number is large. The grid spacing is uniform $\Delta x = \Delta y = 0.01$, and $\Delta t = 5 \times 10^{-5}$. We conduct the simulation until dimensionless time $t = 0.1$. Computed growth rates, V_n, are the averaged ones; i.e., $V_n = \frac{\mathrm{d}\sqrt{A}}{\mathrm{d}t}$, where A is the solid-phase area. Glicksman and Schaefer [33] concluded that the interface is in dendrite form in a moderately supercooled melt ($S < 1$), and "scallops" form in a hypercooled melt ($S > 1$);

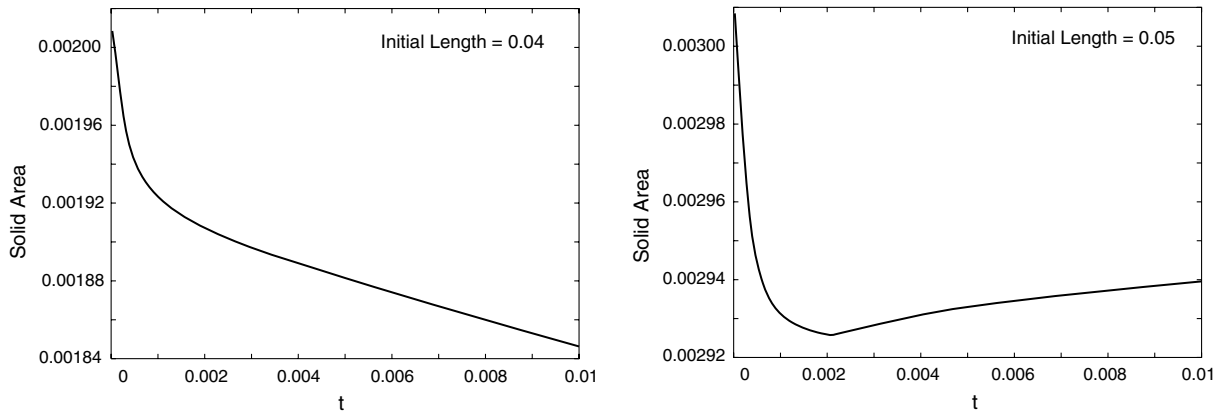

Fig. 8. Solid phase area as a function of time, $S = 0.01$.

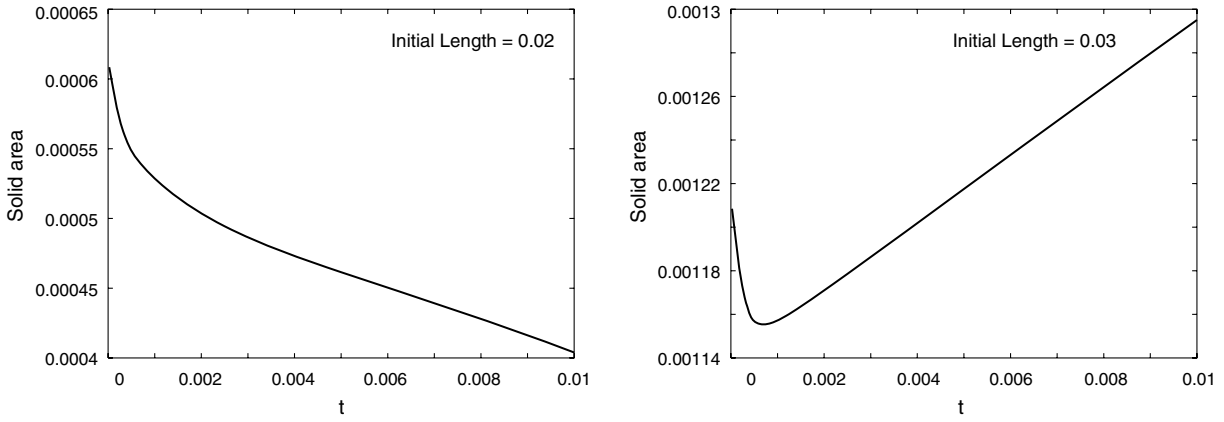

Fig. 9. Solid phase area as a function of time, $S = 0.02$.

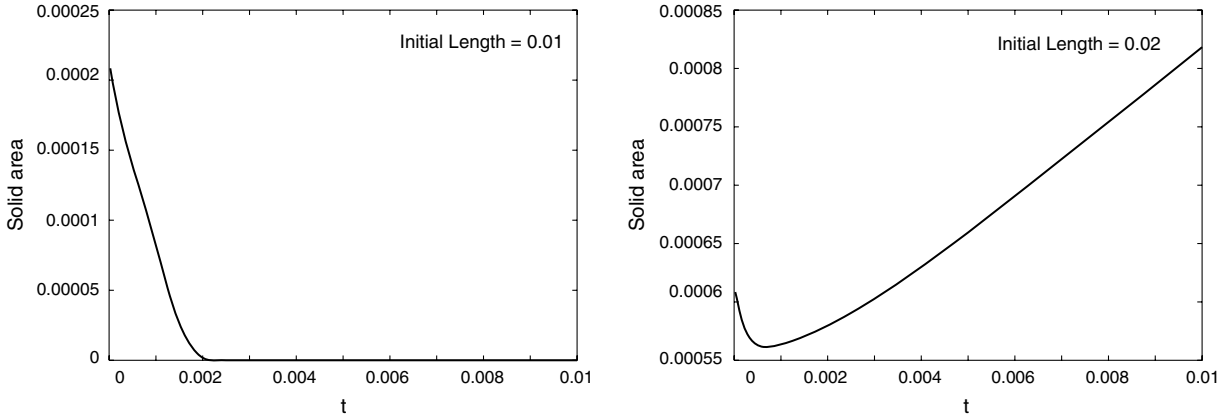

Fig. 10. Solid phase area as a function of time, $S = 0.03$.

then a quasi-planar form (a form of interface with only small curvature) occurs if supercooling is increased further. Fig. 11 illustrates that the computed interface shapes produced by the phase-field model follow these same patterns: interface shapes at time $t = 0.1$ with three different Stefan numbers 0.5, 1.0 and 1.4 are plotted. This provides convincing evidence of the transition from dendritic to "scalloped," and then to the quasi-planar configuration. We could expect that as supercooling continues to increase, the interface becomes almost indistinguishable from a planar interface, from a morphological standpoint.

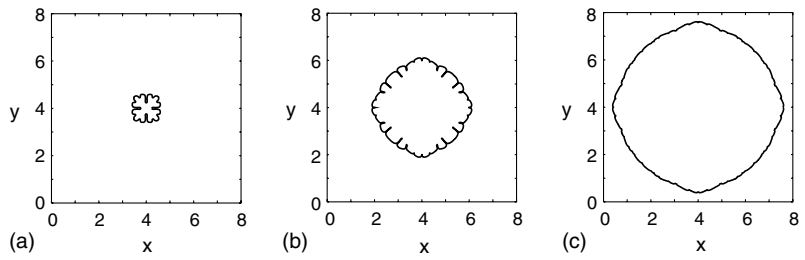

Fig. 11. Interface shapes at $t = 0.1$ for three different Stefan numbers: (a) $S = 0.5$ (dendritic), (b) $S = 1.0$ (scalloped) and (c) $S = 1.4$ (quasi-planar).

The similarity solution of a classical Stefan problem provided in [9,10] indicates that for one-dimensional freezing into a supercooled melt ($S < 1$), interface location as a function of time is $X \sim t^{\frac{1}{2}}$, i.e., $V_n \sim t^{-\frac{1}{2}}$. Moreover, there exists no solution for $S > 1$ because without kinetic supercooling, the heat required to raise the temperature to T_m is higher than the latent heat provided, violating the energy balance. However, in the presence of kinetic supercooling, there are solutions for one-dimensional freezing into a supercooled melt for all $S : X \sim t^{\frac{1}{2}}$ corresponding to $V_n \sim t^{-\frac{1}{2}}$ for $S < 1$, $X \sim t^{\frac{2}{3}}$ corresponding to $V_n \sim t^{-\frac{1}{3}}$ for $S = 1$, and $X \sim t$, and thus $V_n \sim$ constant for $S > 1$ [10]. We observe in the scalings relating V_n and t that the power of t tends to increase with increasing S.

Absence of analytical solutions for two-dimensional freezing into a supercooled melt on a rectangular domain implies that no analytical expression for interfacial speed as a function of time has been obtained. But the computational solutions shown in Fig. 12 provide this relation as follows: for $S < 1$, $0.3t^{-\frac{2}{5}}$ and $2t^{-\frac{2}{5}}$ are used to represent the interfacial speeds for $S = 0.1$ and $S = 0.5$, respectively, to a good approximation over the entire time interval being considered; for $S = 1$, the curve $16t^{-\frac{1}{5}}$ can be used to approximate the computed results; and for $S > 1$ (only results for $S = 1.4$ are shown in Fig. 12), the growth rate is essentially constant at late times. It is clear that the trend is the same as that seen in the 1D analytical solution of Davis [10], that is, we observe an increasing power of t for V_n with the increase of supercooling S, which follows the analytical solution trend.

We note that the power of t is essentially fixed if $S < 0.5$, but increases with S if $0.5 < S < 1.0$ (not shown in Fig. 12). This observation can be explained by the relation between the averaged interfacial speed and the Stefan number displayed in Fig. 13. The existence of a quadratic relationship between V_n and S is related to the lateral mechanism for dendrite growth with $S < 1$ and the continuous mechanism with $S > 1$ by applying Eqs. (12) and (13). This implies that these growth mechanisms are determined by the physical properties of pure

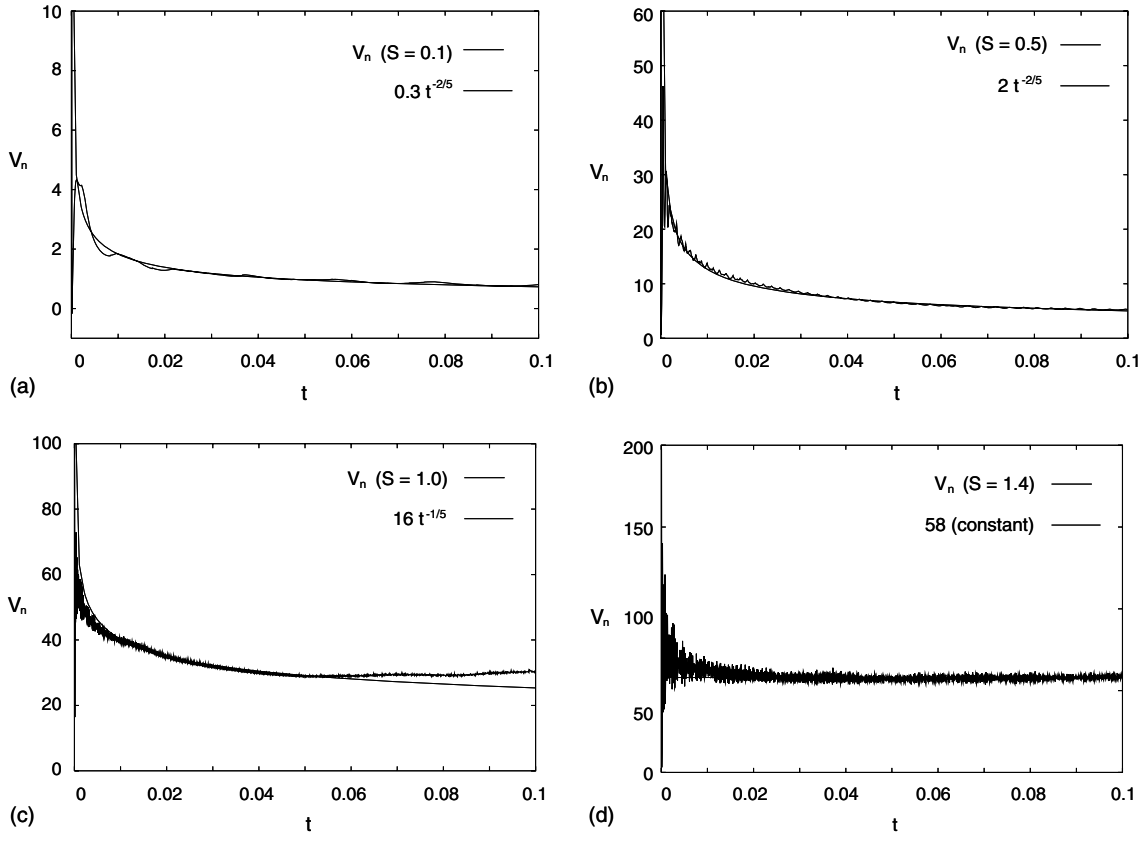

Fig. 12. Computed interfacial speed as a function of time for different Stefan numbers: (a) $S = 0.1$; (b) $S = 0.5$; (c) $S = 1.0$; (d) $S = 1.4$.

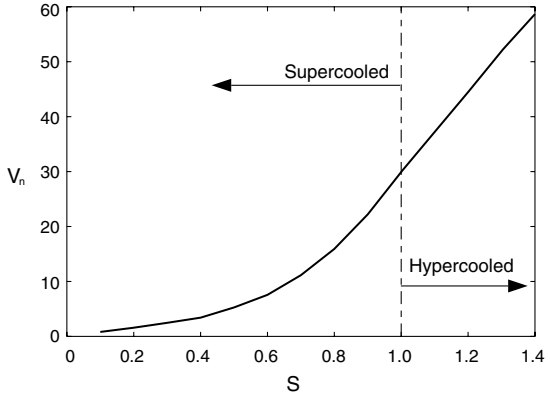

Fig. 13. Computed interfacial speed versus Stefan number at $t = 0.1$.

nickel, and they would be somewhat different for various other materials. The quadratic rather than linear relationship for $S < 1$ also explains why the power of t is increasing as S increases. We also observe that there is no apparent discontinuity in slope in the neighborhood of $S = 1$ in Fig. 13, where the system is transitioning from supercooled to hypercooled. This observation is coincident with the experimental evidence of Glicksman [33] and in conflict with expectations arising from elementary analyses of the classical Stefan problem. Wang and Sekerka [34] investigated the relations between tip velocity and Stefan number using phase-field model at large supercooling. Their results are very similar to our results shown in Fig. 13 for large S.

4.4. Influence of ϵ on the interface

As we mentioned before, a sharp interface model for phase transition problems can be smoothed using the phase-field model. Moreover, the interfacial thickness parameter ϵ is a free parameter, i.e., it can be changed considerably without a significant difference in the development of the interface as noted by Caginalp and Socolovsky [35]. To some extent this is rather counterintuitive, therefore, in this subsection, we conduct several numerical tests to investigate the influence of ϵ on details of the interface, including interfacial speed and interface structure. Space and time step sizes $\Delta x = \Delta y = 0.01$ and $\Delta t = 5 \times 10^{-5}$, respectively, are used. We found that the interface becomes mushy if $\epsilon \geqslant 0.006$, and the numerical scheme is no longer stable if $\epsilon \leqslant 0.001$ for these discrete step sizes. Hence, we display the numerical results for four different values of ϵ: 0.002, 0.003, 0.004 and 0.005. In Fig. 14, we compare interfacial speed versus time for these values of ϵ. The results shown here indicate that the change of interfacial thickness will not significantly alter the interface

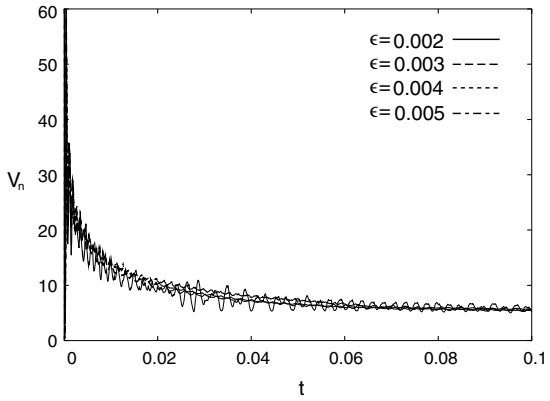

Fig. 14. Computed interfacial speed for different interfacial thickness parameter ϵ at $S = 0.5$.

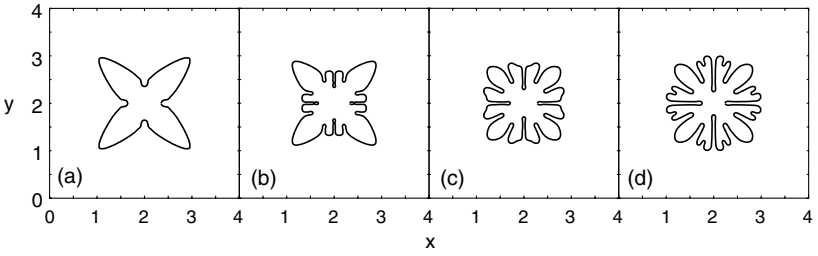

Fig. 15. Interface structure for different interfacial thickness parameter ϵ at $S = 0.5$: (a) $\epsilon = 0.002$; (b) $\epsilon = 0.003$; (c) $\epsilon = 0.004$; (d) $\epsilon = 0.005$.

from the point of view of mean propagation speed. On the other hand, the interface structure changes with ϵ as shown in Fig. 15. We note, however, that since the interface structure is difficult to predict quantitatively, and it changes significantly with perturbations introduced to the system, it does not seem to provide a very suitable property for comparison of the numerical results.

4.5. Effect of initial shape

Fig. 16 presents a sketch of approximating a disk with a union of squares as is necessary on a Cartesian grid. To apply the disk-shaped initial condition generally used, the phase-field value ϕ of the squares inside the circle is assigned a value 0, corresponding to the solid phase. If the distance between a grid point and the disk's center is in the range of $\left[r_d, r_d + \frac{\sqrt{2}}{2}\Delta x\right]$, the phase-field value ϕ of this grid point is also prescribed to be 0. Therefore, the shaded area in Fig. 16 represents the solid phase.

A comparison of Figs. 5 and 17 shows the large difference of the dendrite structure between two different initial shapes, square and round, at all times displayed. The differences are produced by the local curvature of the initial shape. The larger the curvature, the higher the interface velocity. For an ideal disk, the same curvature at every point causes the interface to propagate at the same speed initially, uniformly over its extent. However, since a union of squares is used to approximate the sphere in our case, there exists a difference of curvature from point to point, hence producing dendrites. Moreover, the varieties of rounding error introduced by a square initial shape and a union of squares in the case of round initial shape introduce different fluctuations, and fluctuations are one of the necessities for dendrite formation, which explains the existence of various physical dendrite structures. Thus, the phase-field model is able to mimic even this level of detail.

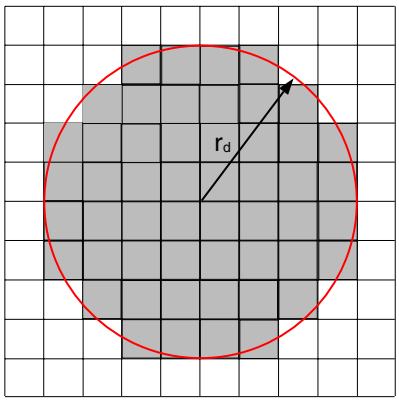

Fig. 16. Approximation to the round initial shape.

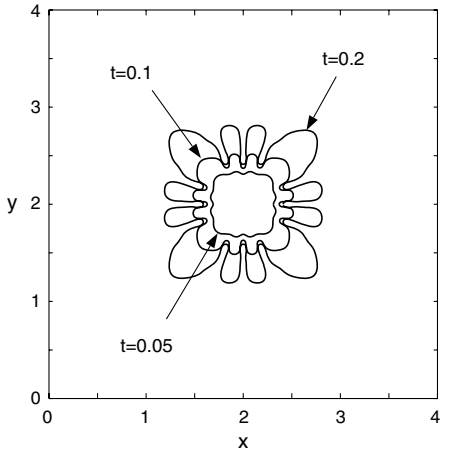

Fig. 17. Dendrite structures for approximately round initial seed at time $t = 0.05$, $t = 0.1$ and $t = 0.2$ (outward direction) with grid size $\Delta x = \Delta y = 0.01$ and $\Delta t = 5 \times 10^{-5}$ for $S = 0.5$ initially with round shape.

5. Summary and conclusions

We have provided a detailed numerical method and algorithm for solving the 2D phase-field model to simulate solidification into a supercooled melt. The computational analysis and results are performed for an isenthalpic system in a square domain. Our computational analyses have focused on the convergence rate of quasilinear iteration, comparison between the fully-coupled and sequential techniques, and the grid function convergence tests. We have also investigated the properties such as dendrite structures, critical radius for nucleation, interfacial growth rates under different degrees of supercooling and the effects of the parameter ϵ and of different initial shapes on evolution of dendrite structure.

The numerical results show that the CPU time of the sequential method is approximate 10% greater than that of the fully-coupled. However, the sequential method is chosen for the current computations to reduce required storage as much as possible. The strong L^2 norm convergence test indicates that the formal second-order accuracy can be obtained. Moreover, evolution of L^2 norm associated with total energy shows that the system energy is numerically conserved.

We found that the numerical results capture the complex physics of solidification problems very well. The computed critical radius convinces us that there exists a critical radius for a nucleus to grow in the phase-field simulation, just as occurs physically. Moreover, the critical radii decrease linearly with increasing Stefan number, which means if the Stefan number is large enough, the solidification always occurs no matter what the initial conditions are. We found that the interfacial growth rate qualitatively agrees with the analytical 1D predictions, and we also determined the crystal growth mechanism of currently-used material nickel by the relationship between the growth rate and the degree of supercooling. Furthermore, the dendrite shapes at different degrees of supercooling are coincident with the experimental results: they display structures ranging from dendritic to scalloped to quasi-planar forms as Stefan number increases.

We will extend our computations to 3D in the future because real physics exists only in 3D. The comparisons between our 3D computational results and experimental data on PVA will be conducted to validate further that the phase-field model captures real physics. In addition, dendrite formation in supercooled liquid in a flow field will be investigated both in 2D and 3D. Moreover, ice formation in a turbulent flow is a very interesting and important work associated with simulating freezing of rivers and oceans. Because such phenomena involve an extremely large range of scales, multi-level formalisms will be needed to efficiently model solidification in such cases.

Acknowledgments

This work was supported by grants from NASA-EPSCoR WKU 522762-98-03 and WKURF 596183-03-09. It was also supported by University of Kentucky Center for Computational Sciences. We are grateful to University of Kentucky Computing Center for providing the HP SuperDome for all computations.

References

[1] G. Fix, Phase field models for free boundary problems, in: A. Fasano, M. Primicerio (Eds.), Free Boundary Problems, Theory and Application, Pitman, New York, 1983, pp. 580–589.
[2] J.S. Langer, Models of pattern formation in first-order phase transitions, in: G. Grinstein, G. Mazenko (Eds.), Directions in Condensed Matter Physics, World Science, Singapore, 1986, pp. 164–186.
[3] G. Caginalp, P. Fife, Phase-field methods for interfacial boundaries, Phys. Rev. B 33 (11) (1986) 7792–7794.
[4] L.D. Landau, V.L. Ginzburg, On the theory of superconductivity, J. Exp. Theor. Phys. (USSR) 20 (1950) 1064.
[5] G. Caginalp, Stefan and Hele–Shaw type models as asymptotic limits of the phase-field equations, Phys. Rev. A 39 (11) (1989) 5887–5896.
[6] G. Caginalp, E.A. Socolovsky, Computation of sharp phase boundaries by spreading: the planar and spherically symmetric cases, J. Comput. Phys. 95 (1991) 85–100.
[7] O. Penrose, P. Fife, Thermodynamically consistent models of phase-field type for the kinetics of phase transitions, Physica D 43 (1990) 44–62.
[8] S.L. Wang, R.F. Sekerka, A.A. Wheeler, B.T. Murray, S.R. Coriell, R.J. Braun, G.B. McFadden, Thermodynamically-consistent phase-field models for solidification, Physica D 69 (1993) 189–200.
[9] V. Alexiades, A.D. Solomon, Mathematical Modeling of Melting and Freezing Processes, Hemisphere Publishing Corp., Washington, DC, 1993.
[10] S.H. Davis, Theory of Solidification, Cambridge University Press, New York, 2001.
[11] A. Karma, W.-J. Rappel, Phase-field method for computationally efficient modelling of solidification with arbitrary interface kinetics, Phys. Rev. E 53 (4) (1996) R3017–R3020.
[12] A. Karma, W.-J. Rappel, Quantitative phase-field modeling of dendritic growth in two and three dimensions, Phys. Rev. E 57 (4) (1998) 4323–4349.
[13] G.B. McFadden, A.A. Wheeler, D.M. Anderson, Thin interface asymptotics for an energy/entropy approach to phase-field models with unequal conductivities, Physica D 144 (2000) 154–168.
[14] R. Kobayashi, Modeling and numerical simulations of dendritic crystal growth, Physica D 63 (1993) 410–423.
[15] A.A. Wheeler, B.T. Murray, R.J. Schaefer, Computation of dendrites using a phase field model, Physica D 66 (1993) 243–262.
[16] A.A. Wheeler, W.J. Boettinger, G.B. McFadden, Phase-field model for isothermal phase transitions in binary alloys, Phys. Rev. A 45 (10) (1992) 7424–7440.
[17] B.T. Murray, W.J. Boettinger, G.B. McFadden, A.A. Wheeler, Computation of dendritic solidification using a phase-field model, ASME Heat Transfer Melting, Solidification Cryst. Growth 234 (1993) 67–76.
[18] Raz Kupferman, Ofer Shochet, Eshel Ben-Jacob, Numerical study of a morphology diagram in the large undercooling limit using a phase-field model, Phys. Rev. E 50 (2) (1994) 1005–1009.
[19] D. Juric, G. Tryggvason, A front-tracking method for dendritic solidification, J. Comput. Phys. 123 (1996) 127–148.
[20] Nikolas Provatas, Nigel Goldenfeld, Jonathan Dantzig, Crossover scaling in dendritic evolution at low undercooling, Phys. Rev. Lett. 82 (22) (1999) 4496–4499.
[21] M.B. Koss, M.E. Glicksman, A.O. Lupulescu, L.A. Tennenhouse, J.C. LaCombe, D.C. Corrigan, J.E. Frei, D.C. Malarik, in: Proceedings of the 36th Aerospace Sciences Meeting, Reno, NV, 1999, AIAA-98-0809.
[22] J. Douglas, J.E. Gunn, A general formulation of alternating direction methods, part I. parabolic and hyperbolic problems, Numer. Math. 6 (1964) 428–453.
[23] W.F. Ames, Numerical Methods for Partial Differential Equations, Academic Press, New York, NY, 1977.
[24] Ying Xu, Tianliang Yang, J.M. McDonough, K.A. Tagavi, Parallelization of phase-field model for phase transformation problem, in: B. Chetverushkin et al. (Eds.), Proceedings of the Parallel CFD 2003 Conference, Moscow, Russia, May, 2003, pp. 213–218.
[25] R. Ueda, J.B. Mullin (Eds.), Crystal Growth and Characterization, American Elsevier Publishing Co. Inc., New York, 1975.
[26] C. Beckermann, H.-J. Diepers, I. Steinbach, A. Karma, X. Tong, Modeling melt convection in phase-field simulations of solidification, J. Comput. Phys. 154 (1999) 468–496.
[27] W. Kurz, D.J. Fisher, Fundamentals of Solidification, Trans Tech Publications, Switzerland, 1998.
[28] P. Papon, J. Leblond, P.H.E. Meijer, The Physics of Phase Transitions: Concepts and Applications, Springer, Berlin, Germany, 2002.
[29] John W. Cahn, Theory of crystal growth and interface motion in crystalline materials, Acta Metall. 8 (1960) 554–562.
[30] John W. Cahn, W.B. Hillig, G.W. Sears, The molecular mechanism of solidification, Acta Metall. 12 (1964) 1421–1439.
[31] W.B. Hillig, Kinetics of solidification from nonmetallic liquids, in: W.D. Kingery (Ed.), Kinetics of High Temperature Processes, Wiley, New York, 1958, pp. 127–135.
[32] Eric A. Brandes (Ed.), Smithells Metals Reference Book, sixth ed., Butterworth, London, 1983.

[33] M.E. Glicksman, R.J. Schaefer, Investigation of solid/liquid interface temperatures via isenthalpic solidification, J. Cryst. Growth 1 (1967) 297–310.
[34] Shun-Lien Wang, Robert F. Sekerka, Computation of the dendritic operating state at large supercoolings by the phase field model, Phys. Rev. E 53 (4) (1996) 3760–3776.
[35] G. Caginalp, E.A. Socolovsky, Efficient computation of a sharp interface by spreading via phase field methods, Appl. Math. Lett. 2 (2) (1989) 117–120.